SUPPORTING INFORMATION

Bacterial Quorum Sensing Signals Self-Assemble in Aqueous Media to Form Micelles and Vesicles: An Integrated Experimental and Molecular Dynamics Study

Curran G. Gahan,[1,†] Samarthaben J. Patel,[1,†] Michelle E. Boursier,[2,‡] Kayleigh E. Nyffeler,[2] James Jennings,[1,§] Nicholas L. Abbott,[1,#] Helen E. Blackwell,[2,*] Reid C. Van Lehn,[1,*] and David M. Lynn[1,2,*]

[1]Dept. of Chemical and Biological Engineering, Univ. of Wisconsin–Madison, 1415 Engineering Dr., Madison, WI 53706; [2]Dept. of Chemistry, Univ. of Wisconsin–Madison, 1101 University Ave., Madison, WI 53706, USA; [‡]Current address: Amgen, Inc., 1 Amgen Center Dr., Thousand Oaks, CA 91320; [§]Current address: Department of Chemistry, University of Sheffield, S11 8RZ, United Kingdom [#]Current address: Smith School of Chemical and Biomolecular Engineering, Cornell Univ., Ithaca, NY 14853; [†]Equally contributing author; Email: (H.E.B.) blackwell@chem.wisc.edu; (R.C.V.) vanlehn@wisc.edu; (D.M.L.) dlynn@engr.wisc.edu

Contents.

Section S1. Additional details related to the measurement and calculation of experimental critical aggregation concentration (CAC)

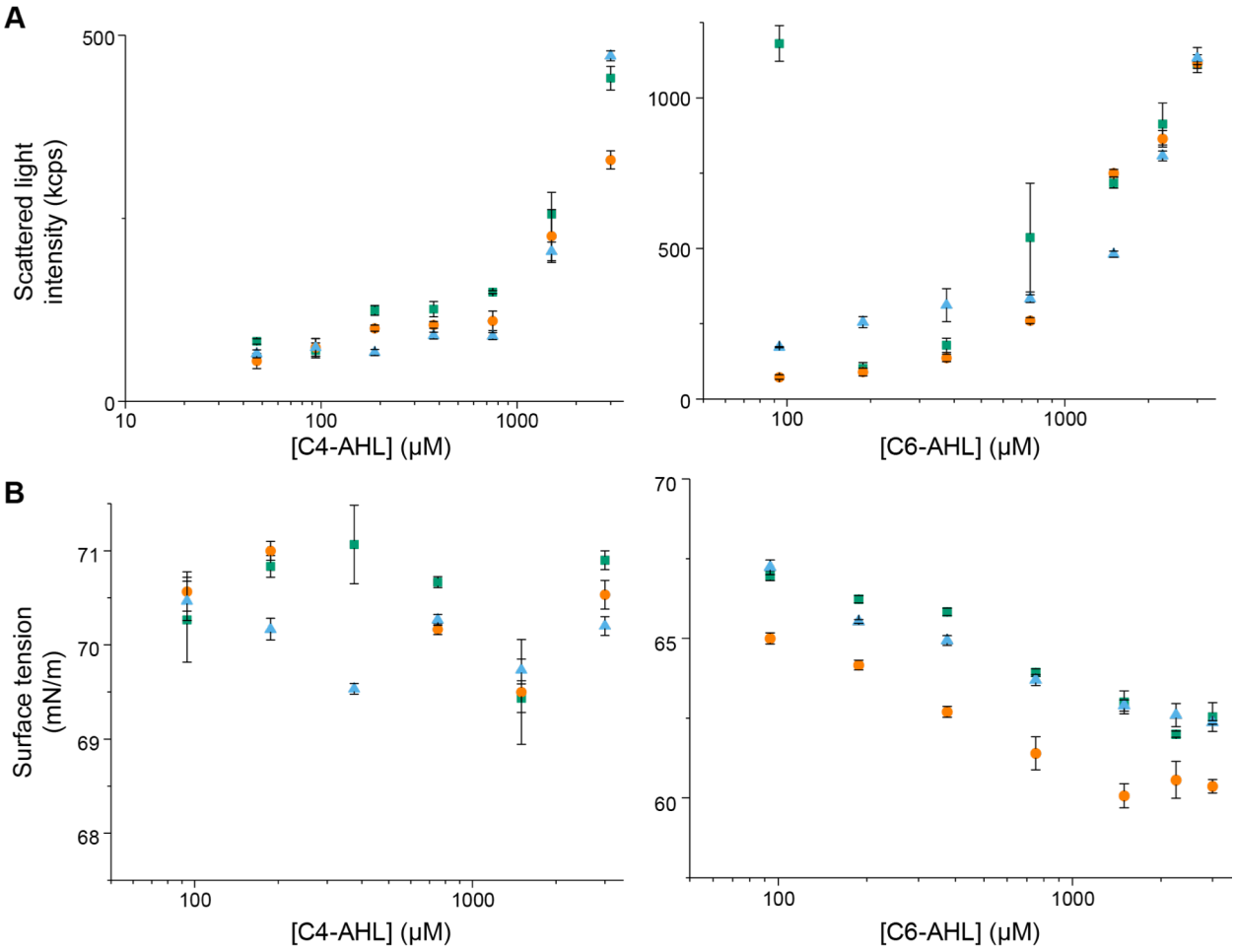

Figure S1. Static light scattering and surface tension data for C4-AHL and C6-AHL. A) Plots of scattered light intensity of a 532 nm incident laser, detected at 173°, at various concentrations of these two AHLs in distilled water containing 1% DMSO at 30 °C. B) Plots showing the surface tensions of solutions at various concentrations of these two AHLs in distilled water containing 1% DMSO at ambient room temperature. All points represent the average and standard deviation of three independent measurements of a single sample. Green, orange, and blue data points show results obtained for three sets of independently prepared samples.

Figure S1 shows the scattered light intensity (Figure S1A) and surface tension (Figure S1B) measured for solutions of C4-AHL and C6-AHL at various concentrations. While the intensity of scattered light increased with increasing concentration of both C4-AHL and C6-AHL, regressions of the scattered light intensity against concentration yielded very low CAC values (near zero or negative concentrations). These measured values of CACs are either unphysical or do not follow trends commonly observed for self-assembled amphiphiles, for which the CAC

typically decreases with increasing tail length. Additionally, C4-AHL exhibited little surface activity, with any change in the surface tension of solutions of this AHL appearing to be random at increasing concentrations. This result suggests a lack of amphiphilicity. While C6-AHL does exhibit surface activity, the surface tension and light scattering assays do not agree with one another, as regression of two of the three light scattering trials returned negative CAC values and the third (~200 μM) did not correspond to the concentrations at which surface tension was observed to become constant in the three surface tension trials (~1500 μM). General agreement between these two assays was observed for the other AHLs investigated (see main text), consistent with cooperative self-assembly. While the data discussed here leave open the possibility that some form of assembly or aggregation is occurring in solutions of C4-AHL and C6-AHL, the behaviors of these compounds deviates from those of longer-tailed AHLs, and we cannot confidently determine whether this behavior is driven by cooperative self-assembly.

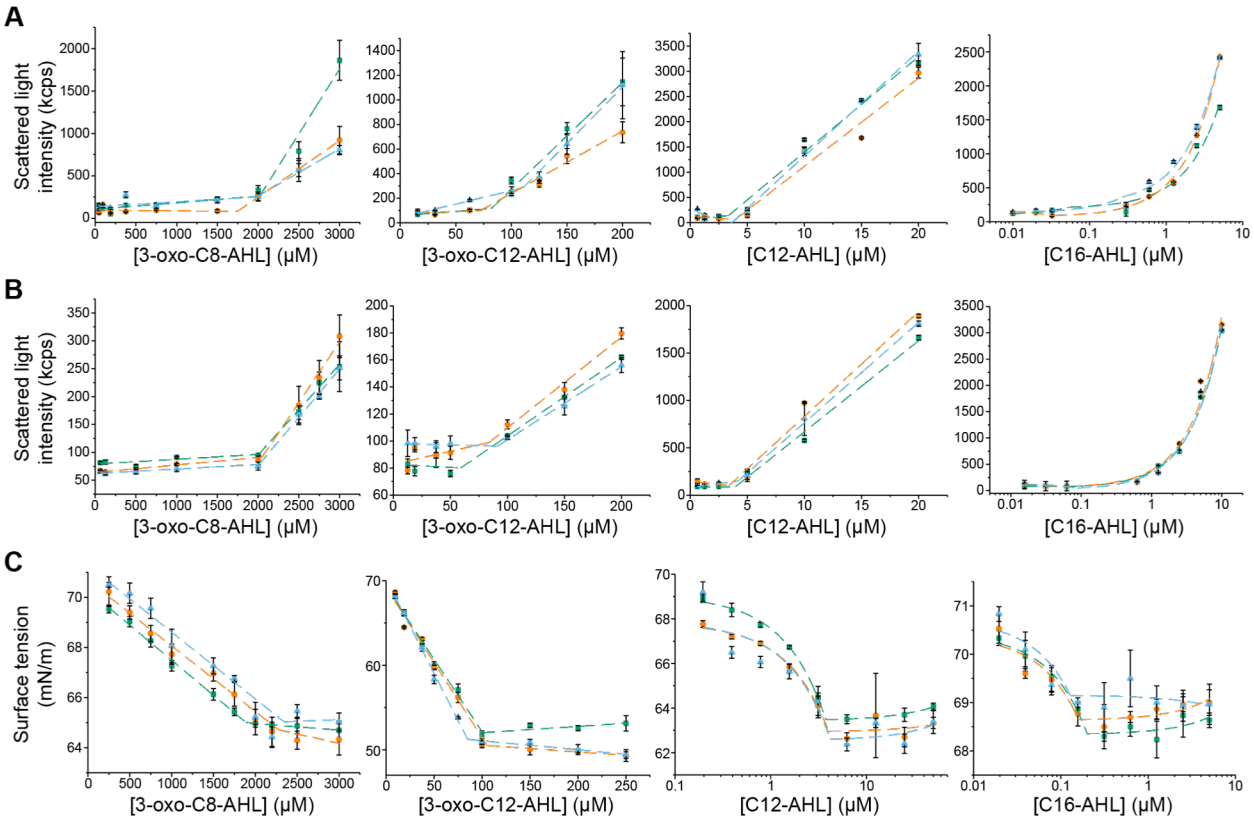

Figure S2. Determination of the CAC of 3-oxo-C8-AHL, 3-oxo-C12-AHL, C12-AHL, and C16-AHL using static light scattering and measurements of surface tension in aqueous media containing 1% DMSO. All points represent the average and standard deviation of three independent measurements of individual solutions of AHLs. Green, orange, and blue data points show results obtained for three sets of independently prepared samples. Note that AHL concentrations in some panels are plotted on a log scale. A) Plots of scattered light intensity of a 532 nm incident laser, detected at 173°, at various concentrations of AHLs in distilled water at 30 °C. B) Plots of scattered light intensity of a 532 nm incident laser, detected at 173° at various concentrations of AHLs in LB medium at 37 °C. C) Plots of the surface tensions of solutions of various concentrations of AHLs in distilled water at ambient room temperature.

Figure S2 shows the complete set of static light scattering and surface tension data used to determine the CACs listed in Table 1 of the main text. Linear regressions of scattered light intensity and surface tension against concentration were performed separately for the points above and below the concentration at which either (*i*) the scattered light intensity of AHL solutions began to increase at increasing AHL concentrations, or (*ii*) further increasing the concentration of AHLs in solution did not further decrease the surface tension of the solution. The CAC for each AHL was defined as the concentration corresponding to the intersection of the regression lines. Measurement error (standard deviations of three measurements of an individual sample) was generally small compared to inter-sample deviation (differences in the average values of three individual samples at the same concentration). Measurement error was therefore not included in the error associated with the CACs. The CACs reported in Table 1 are the averages and standard deviations of the three samples.

As stated in the main text and reiterated here, we note that the concentrations of AHLs in solution and their corresponding changes in surface tension are small when compared to other common surfactants characterized using this assay.[1-3] This suggests that there is a low surface coverage of AHLs at the interface, likely due to the low concentrations at which the CACs occur. These low surface coverages could explain why a very small linear region was observed when surface tension is plotted against the logarithm of concentration (which for some trials, when regressed, measured a value of the CAC that was larger than the highest concentration of AHL measured). A linear regression of surface tension against concentration gave a better fit to the data and yielded CAC values that were consistent with those measured by static light scattering. This approach was therefore was used to analyze these surface tension data for the determination of a CAC.

We note that the changes in surface tension observed for solutions of C16-AHL are small even in comparison with the other AHLs tested here, likely due to the low CAC of the molecule. However, the concentration at which the surface tension becomes constant for C16-AHL does agree generally with the CACs determined using light scattering in both water and LB medium.

Section S2. Zeta potential measurements

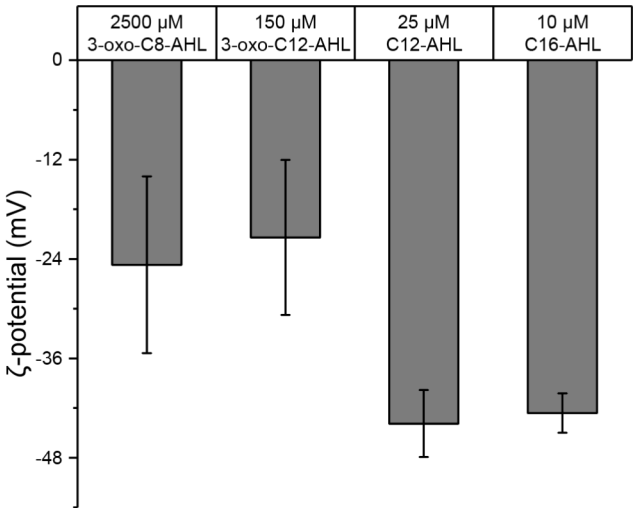

Figure S3. Zeta potentials measured for 2500 µM 3-oxo-C8-AHL, 150 µM 3-oxo-C12-AHL, 25 µM C12-AHL, and 10 µM C16-AHL solutions in distilled water containing 1% DMSO at room temperature. Values shown are the averages and standard deviations of seven to 10 measurements made of three independent samples.

Section S3. Details related to preparation of simulation systems

Initial configurations of spherical, cylindrical, and bilayer aggregates used for alchemical free energy calculations were generated using PACKMOL.[4] All aggregates were prepared by packing the AHLs into the desired geometry with head groups oriented away from the aggregate center. The cylindrical aggregates were formed with the principal axis aligned with the *z*-axis. The bilayers were formed with the surface normal aligned with the *z*-axis. The PACKMOL-generated spherical aggregate and bilayer systems were solvated with water, energy minimized, and equilibrated as stated in the main text, whereas a more elaborate approach was used to equilibrate the cylindrical aggregates as further described in Section S4 below. Figure S4 shows snapshots of example systems prepared using PACKMOL.

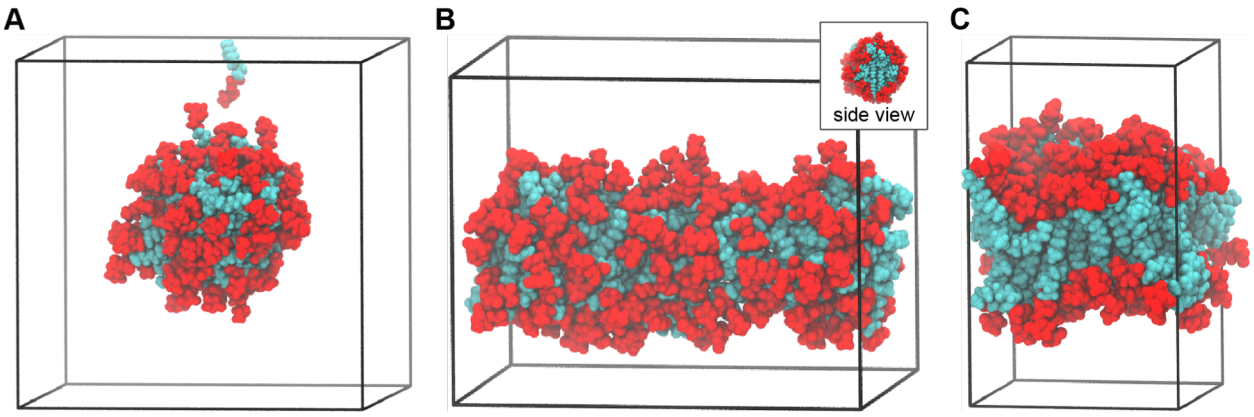

Figure S4. Simulation snapshots of PACKMOL-generated configurations at the end of equilibration for 3-oxo-C12-AHL aggregates. The color scheme is the same as Figure 4 of the main text and water is omitted for clarity. A) Spherical aggregate containing 100 AHLs. B) Cylindrical aggregate containing 150 AHLs. The inset shows the side view of the aggregate. C) Bilayer containing 128 AHLs.

Section S4. Preparation of simulated cylindrical aggregates

Preliminary simulations found that cylindrical aggregates simulated with semi-isotropic pressure coupling were not stable and deformed by compression along the long axis of the cylindrical aggregate. This behavior has been observed in previous literature.[5] An example of the resulting highly compressed structure is shown in Figure S5A. This aggregate displays AHL packing similar to that of a bilayer, which might indicate that the cylindrical aggregate is not the thermodynamically favorable structure. However, we sought to confirm this finding for all AHLs by developing a workflow to prepare stable cylindrical aggregates to facilitate the calculation of aggregation free energies.

In the modified workflow, we equilibrated the solvated PACKMOL-generated cylindrical aggregates for 30 ns using a semi-isotropic Berendsen barostat with a time constant of 5 ps and a compressibility of 4.5×10^{-5} bar^{-1}. All other parameters were the same as those stated in the main text. We then selected a single configuration from the resulting trajectory and performed an additional 50 ns of equilibration, initialized from the selected configuration, using an isotropic Berendsen barostat (again with a time constant of 5 ps and a compressibility of 4.5×10^{-5} bar^{-1}) to prevent compression along a single axis. The configuration from the initial equilibration trajectory was selected based on two criteria: (1) the head group area in the cylindrical aggregate should be approximately the average of the head group area for the spherical aggregates and the head group area for the bilayer, and (2) the structure should be cylindrical, with head groups localized to the outer surface of the cylinder and tail carbon atoms located on the cylinder interior. We rationalized criterion (1) based on packing – the packing parameter for a cylinder lies between that of a spherical micelle and a bilayer and is inversely proportional to the head group area.[6]

To satisfy criterion (1), we estimated the head group area per AHL for the spherical and the bilayer aggregates from the last 5 ns of their equilibration trajectories. For the spherical aggregates, we first computed the density of nitrogen atoms in the AHL head groups as a function of the radial distance from the center of the aggregate and defined the radius of the aggregate as the radial distance corresponding to the peak of this distribution (as shown in Figure S5B). The head group area was then defined as the surface area of a sphere with this radius divided by the total number of AHLs in the aggregate. This head group area was averaged across the values obtained for spherical aggregates containing 20, 50, and 100 AHLs. The head group area per AHL for the bilayer was calculated by dividing the area of the of the simulation box in the *x*-*y* plane (the plane spanned by the bilayer) by one-half of the total number of AHLs in the bilayer. The expected head group area per AHL in the cylindrical aggregate was then obtained by averaging the head group area per AHL for the spherical aggregates and the bilayer. We next estimated the head group area for the cylindrical aggregate for each configuration in the semi-isotropic pressure coupling equilibration trajectory (as shown in Figure S5C). As with the spherical aggregates, we computed the density of nitrogen atoms as a function of the radial distance from the center of the aggregate (projected into the *x*-*y* plane since the cylinder was aligned with the *z*-axis) and defined the cylinder's radius as the radial distance corresponding to the peak of this distribution. The head group area per AHL was then defined by calculating the

surface area of a cylinder with this radius and dividing by the total number of AHLs. Using this approach, we selected the first configuration for which the head group area per AHL matched the expected value.

To satisfy criterion (2), we calculated the two-dimensional radius of gyration in the *x*-*y* plane using either the head group nitrogen atoms or the last tail carbon atoms using the GROMACS function *gmx gyrate*. The radius of gyration was calculated for 10 separate slices of the box along the *z*-axis to account for any curvature along the length of the aggregate. If the aggregate is cylindrical, then the radius of gyration calculated using the head group atoms should be larger than the radius of gyration computed using the tail carbon atoms; hence, we subtracted the radius of gyration calculated using the tail carbon atoms from the radius of gyration computed using the nitrogen atoms to determine if the configuration that was selected to satisfy criterion (1) also satisfies criterion (2). If the difference was greater than zero for all ten slices, then we accepted the selected configuration (as indicated by the dashed red line in Figure S5D; an example snapshot of such configuration is shown in Figure S4B) and performed the isotropic pressure coupling equilibration. If the difference was zero or negative, we selected the first configuration from an earlier time point in the trajectory for which the difference was greater than zero for all slices.

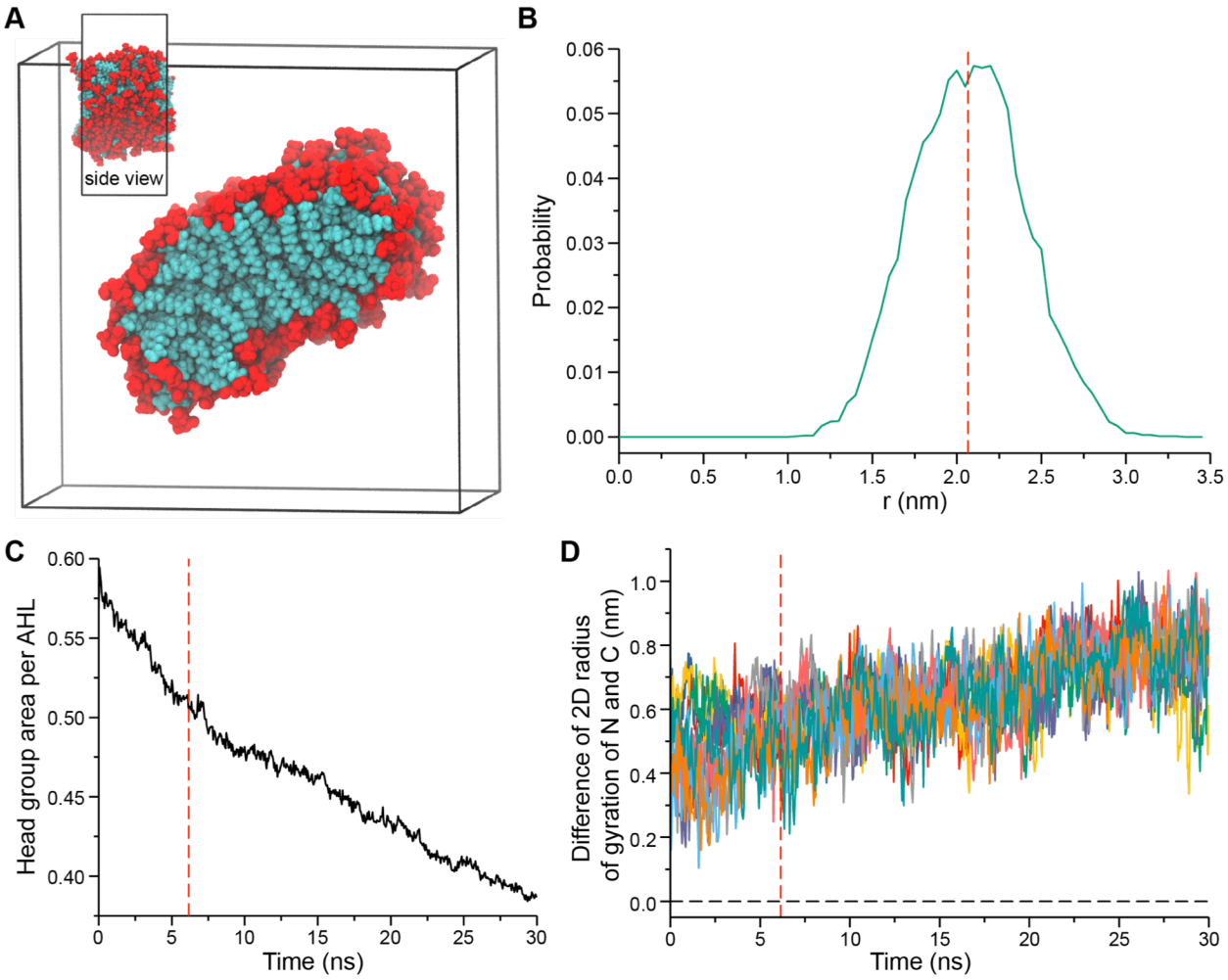

Figure S5. A) Snapshot of a C12-AHL aggregate that was initially prepared as a cylinder with 200 molecules at the end of a 40 ns equilibration trajectory using semi-isotropic pressure coupling. The color scheme is the same as Figure 4 of the main text and water is not shown for clarity. The aggregate is notably compressed along the long-axis and loses its initial cylindrical structure. B) Distribution of head group nitrogen atom distances from the aggregate center for a C12-AHL spherical aggregate with 100 molecules. The distribution was computed using the last 5 ns of the equilibration trajectory. The dashed red line indicates the radius of the aggregate used to calculate the surface area of the aggregate. C) Head group area per AHL calculated during the semi-isotropic pressure coupling equilibration trajectory for the C12-AHL cylindrical aggregate shown in part A. The dashed red line indicates the configuration selected for the isotropic pressure coupling equilibration trajectory. D) Difference between the two-dimensional radii of gyration computed using the nitrogen atoms and the tail carbon atom for the C12-AHL equilibration trajectory from part A. Each solid line indicates the calculation for one of ten different slices along the *z*-axis. The dashed red vertical line indicates the configuration selected for the isotropic pressure coupling equilibration trajectory.

Section S5. Details related to alchemical free energy calculations

The free energy change for aggregation, $\Delta\mu_{aggr}$, was calculated according to Equation (3) of the main text using the thermodynamic cycle indicated in Figure 2 of the main text. The free energy for removing a single AHL molecule from water, $-\Delta G_{0\to w}$, was calculated using an alchemical free energy approach in which the electrostatic and van der Waals interactions between the AHL and water were separately decoupled in 21 simulation windows. Electrostatic interactions were decoupled in 5 windows using a linear alchemical pathway with λ_{elec} = 0.0, 0.25, 0.5, 0.75, and 1.0, with $\lambda_{vdw} = 0.0$ in each window. Van der Waals interactions were decoupled in 16 windows in which λ_{vdw}= 0.0, 0.1, 0.2, 0.3, 0.4, 0.45, 0.5, 0.55, 0.6, 0.65, 0.7, 0.75, 0.8, 0.85, 0.9, 0.95, and 1.0, with λ_{elec}= 1.0 in each window.

The free energy for removing an AHL from an aggregate, $-\Delta G_{0\to agg}$, was similarly calculated using an alchemical free energy calculation by decoupling the interactions of a single AHL in an aggregate with solvent molecules and other AHLs. During these simulations, the elimination of interactions between the selected AHL and other AHLs in some simulation windows permitted the diffusion of the AHL out of the aggregate and into solution, which leads to poor convergence of the free energy. To prevent this issue, restraints were used to ensure that the AHL being decoupled remained within the aggregate. The free energy change associated with adding and removing these restraints must then be included in the total free energy calculations. Thus, $-\Delta G_{0\to agg}$ is calculated by adding the free energies for decoupling the electrostatic ($\Delta G^{elec}_{agg\to 0}$) and the van der Waals ($\Delta G^{vdw}_{agg\to 0}$) interactions of an AHL in an aggregate, along with free energies for applying restraints before decoupling the AHL ($\Delta G^{add\ rest}_{agg\to 0}$) and removing the restraints after decoupling the AHL ($\Delta G^{rem\ rest}_{agg\to 0}$), according to Equation S1:

$$-\Delta G_{0\to agg} = \Delta G^{add\ rest}_{agg\to 0} + \Delta G^{elec}_{agg\to 0} + \Delta G^{vdw}_{agg\to 0} + \Delta G^{rem\ rest}_{agg\to 0} \quad \text{(S1)}$$

Restraints were applied using a harmonic potential with details on the parameters for the restraints detailed in Section S6. $\Delta G^{add\ rest}_{agg\to 0}$ was calculated using 3 windows with λ_{rest} = 0.0, 0.75, and 1.0 and $\lambda_{elec} = \lambda_{vdw} = 0.0$ in each window. With $\lambda_{rest} = 1.0$ (*i.e.*, with restraints applied), the electrostatic interactions were then decoupled using a linear alchemical pathway with λ_{elec} = 0.0, 0.25, 0.5, 0.75, and 1.0 and $\lambda_{vdw} = 0.0$ in each window. Van der Waals interactions were then decoupled with λ_{vdw}= 0.0, 0.05, 0.1, 0.15, 0.2, 0.25, 0.3, 0.35, 0.4, 0.45, 0.5, 0.55, 0.6, 0.65, 0.7, 0.75, 0.8, 0.85, 0.9, 0.95, and 1.0, with λ_{elec}= 1.0 in each window. A total of 27 windows were utilized for each calculation. The free energy change for removing the restraints, $\Delta G^{rem\ res.}_{agg\to 0}$, was calculated analytically using Equation S2[7]:

$$\Delta G^{rem\ rest}_{agg\to 0} = -RT \ln \left[\frac{V^o}{V^{\text{eff}}}\right] \quad \text{(S2)}$$

Since the restraints are removed from a molecule that has no interactions with other molecules in the system, this expression is the free energy change associated with increasing the volume accessible to an ideal gas molecule. V^o = 1.661 nm^3 is the standard state volume and

V^{eff} is the effective volume of the restrained molecule, which is calculated for each aggregate shape based on the volume accessible to an ideal gas molecule subject to a harmonic restraint with spring constant *k*. For spherical aggregates, V^{eff} was calculated using Equation S3:

$$V^{\text{eff}} = 4\pi \left\{ \int_0^\infty r^2 \exp\left(-\frac{k}{2RT}(r - r^o)^2 \right) dr \right\} \tag{S3}$$

r^o is the equilibrium distance from the center of the sphere enforced by the restraint. For bilayers, the harmonic potential was applied in the *z*-direction and V^{eff} was calculated using Equation S4:

$$V^{\text{eff}} = A \left\{ \int_{-\infty}^\infty \exp\left(-\frac{k}{2RT}(z - z^o)^2 \right) dz \right\} \tag{S4}$$

A is the area of the *x*-*y* plane and z^o is the equilibrium distance from the center of the bilayer enforced by the restraint. For cylindrical aggregates, the harmonic potential was applied in the *x*-*y* plane and V^{eff} as calculated using Equation S5:

$$V^{\text{eff}} = 2\pi L \left\{ \int_0^\infty r \exp\left(-\frac{k}{2RT}(r - r^o)^2 \right) dr \right\} \tag{S5}$$

L is the average length of the cylinder and r^o is the equilibrium distance from the center of the sphere enforced by the restraint (calculated in the *x*-*y* plane). Additional details on the values of *k*, r^o, and z^o for each system are provided in Section S6.

For each simulation window of either an AHL in an aggregate or in solution, the initial configuration was energy minimized, then equilibrated in the NVT ensemble for 500 ps, then equilibrated in *NPT* ensemble for 500 ps. Simulation parameters for the alchemical free energy simulations were the same as for the unbiased equilibration simulations, expect a stochastic dynamics algorithm was used to integrate the equations of motion. The temperature was maintained at 310.15 K with a time constant of 1.0 ps, and the pressure was maintained at 1 bar using a Parrinello-Rahman barostat with a time constant of 5 ps and a compressibility of 4.5×10^{-5} bar^{-1}. After equilibration, each window was simulated for 8 ns, except for POPC for which it was for 24 ns because it is a larger molecule compared to the AHLs. Free energies were computed from the simulation windows using the Multistate Bennett Acceptance Ratio (MBAR) method.[8] The convergence of the alchemical free energy calculations was assessed using a protocol described in the literature.[9] The free energy was calculated using simulation configurations extracted consecutively starting from the beginning of the simulation trajectory (labeled as the "forward" time series) and separately from the same number of consecutive configurations consecutively extracted starting from the end of the simulation trajectory (labeled as the "reverse" time series). Figure S6 plots forward and reverse free energy calculations for a single C12-AHL molecule in water and all five C12-AHL aggregates. Convergence is observed by a simulation time fraction of ~0.9 for all examples in Figure S6.

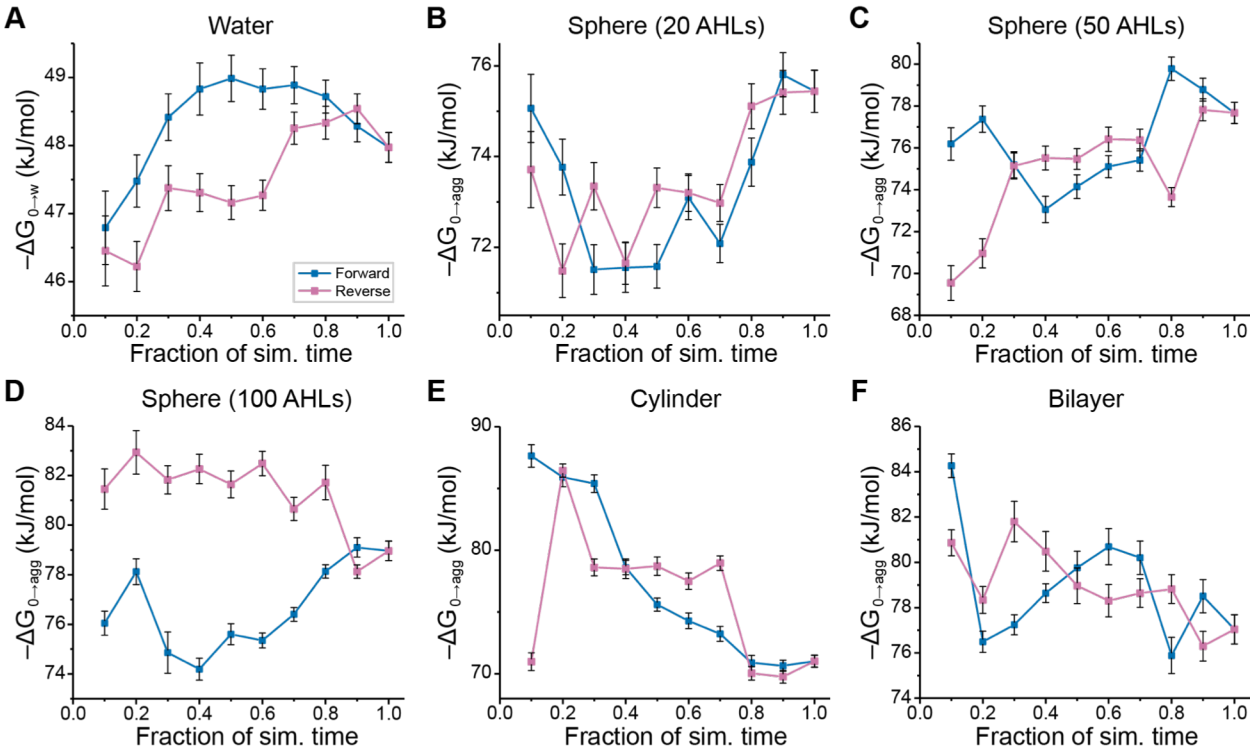

Figure S6. Representative plots illustrating the convergence of alchemical free energy calculations using the forward and the reverse time series of the C12-AHL in water (A), for the spherical aggregates with 20 (B), 50 (C), and 100 (D) AHLs, for the cylindrical aggregate (E), and for the bilayer (F).

Section S6. Aggregate structures and harmonic restraint parameters for free energy calculations

Distributions of the AHL center-of-mass (COM) distance from the aggregate COM were computed for each aggregate structure to assess equilibration and determine parameters for the harmonic restraints applied during the free energy calculations. For cylindrical aggregates, the COM distance was projected onto the *x*-*y* plane, or the plane perpendicular to the axis of the aggregate. For bilayers, the distance was projected onto the *z*-axis, or the axis normal to the bilayer. Distributions were computed separately using either the last 10 ns of the equilibration trajectory or two separate 5-ns blocks taken from the last 10 ns to assess convergence. If the three distributions nearly overlap, the system is equilibrated and the aggregate shape is well-defined. Distributions of C12-AHL COMs are shown in Figure S7 as an example of well-equilibrated structures. Similar calculations were performed to confirm convergence for all AHLs studied.

The spring constant, k, and the distance at which the AHL was restrained during the alchemical free energy calculations were defined separately for each aggregate based on the distributions of AHL COM distances computed during the equilibration trajectories. We defined r^o (Equations S3 and S5) as the distances in the radial direction (for spherical and cylindrical aggregates) and z^o (Equation S4) as the distance along the *z*-axis (for bilayers) corresponding to the peak in the distribution computed for each system from the last 5 ns of the equilibration run. The same distributions were then fitted with Gaussian curves to obtain an estimate of the spring constant value required for the harmonic restraints applied during the alchemical free energy calculation. This approach ensures that the restrained AHL molecule with all interactions decoupled still samples the same conformational space as unrestrained, fully interacting AHLs. Figure S7F shows an example Gaussian fit is plotted for the 20-molecule sphere of C12-AHL and the corresponding distribution of the AHL COM distance from the last 5 ns of a 50 ns restrained simulation using the spring constant, k, obtained from the Gaussian fitting procedure. This comparison confirms that the calculated spring constant used for the alchemical free energy calculation reproduces the expected distribution of AHL COM distances even when intermolecular interactions are decoupled.

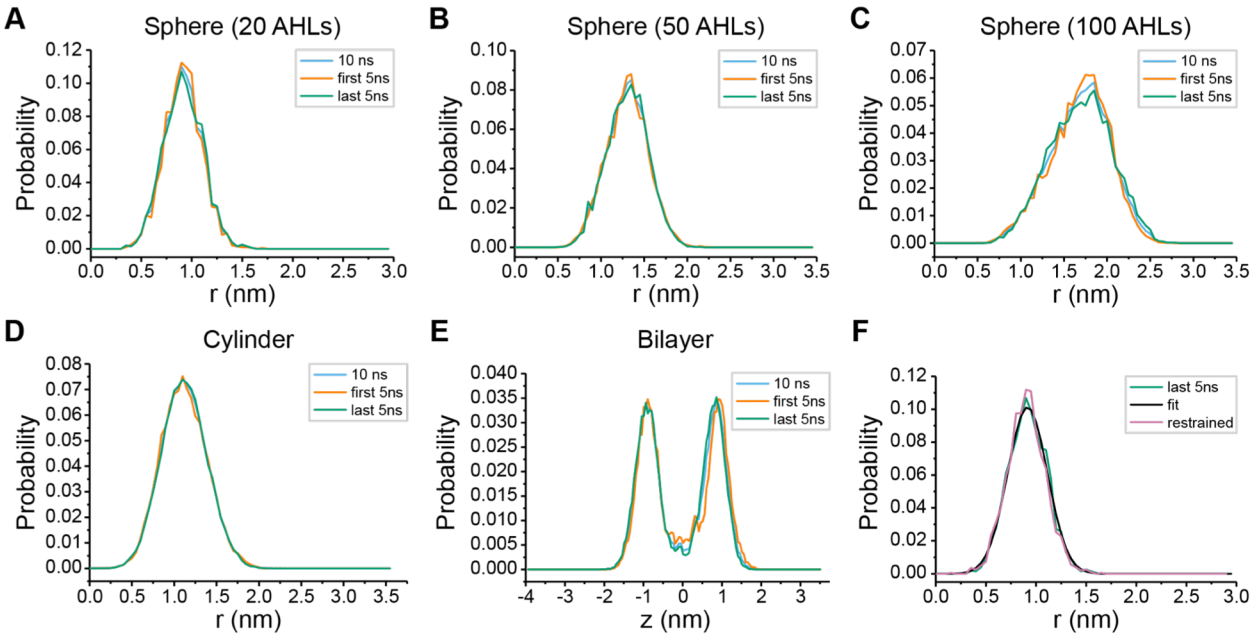

Figure S7. Distributions of the C12-AHL center-of-mass (COM) distance from the aggregate center for spherical aggregates with 20 (A), 50 (B), and 100 (C) AHLs and for the cylindrical aggregate (D) and bilayer (E). Blue, orange, and green curves represent distributions computed from the last 10 ns of the equilibration trajectory, or the 10-ns split into two 5-ns blocks. F) A Gaussian fit of the distribution of C12-AHL COM distances for the 20 molecule spherical aggregate (black line), computed using the last 5 ns of the equilibration trajectory (green line in A) and distribution of C12-AHL COM distance for the 20 molecule spherical aggregate from the last 5 ns of a restrained simulation run using the distance at which the AHL was restrained and the spring constant, *k*, obtained from the Gaussian fitting (purple line).

Section S7. Determination of shape and size of spherical aggregate from simulations

To quantify the shape of each spherical aggregate we calculated the asphericity, α_s, following previous work.[10] The asphericity is defined in Equation S6 as:

$$\alpha_s = \frac{(I_1 - I_2)^2 + (I_1 - I_3)^2 + (I_2 - I_3)^2}{\frac{1}{2}(I_1 + I_2 + I_3)^2} \quad \text{(S6)}$$

I_1, I_2, and I_3 are moments of inertia for the structure, defined such that $I_1 \leq I_2 \leq I_3$. The moments of inertia of the aggregates were calculated using *gmx principal* using the last 10 ns of the equilibration of the spherical aggregates. Figure S8A reports values of α_s obtained by averaging over configurations from the last 10 ns of the equilibration trajectory. α_s values close to zero indicate that the corresponding aggregates are more spherical. This plot indicates that for nearly all AHLs the asphericity increases once the aggregate contains 100 molecules, suggesting that the aggregates containing 20, 50, and 100 AHLs samples a reasonable range of asphericities.

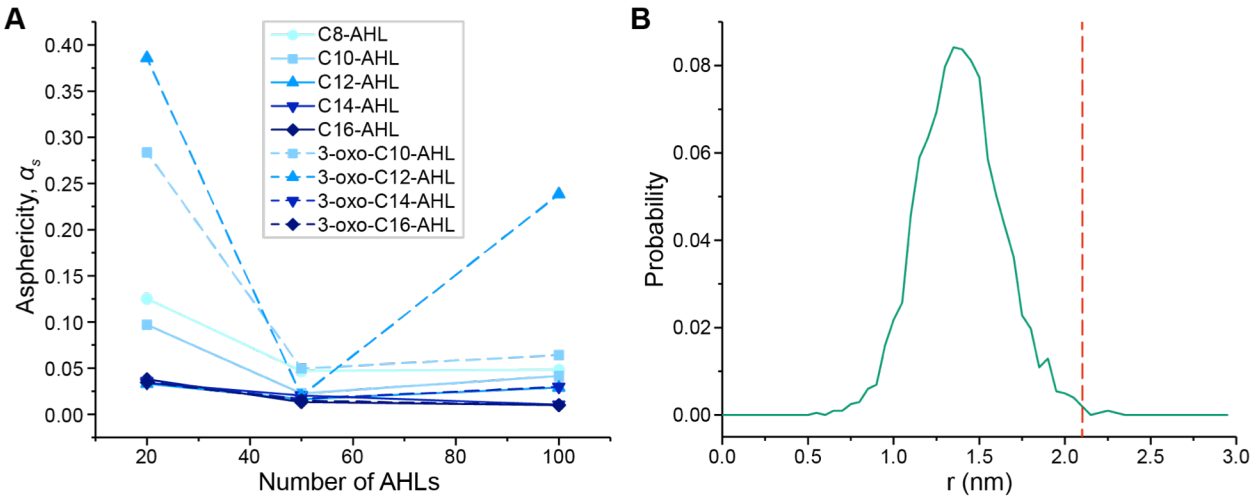

Figure S8. A) Asphericity as a function of number of AHLs in spherical aggregates. B) Distribution of head group lactone ring oxygen atom distances from the aggregate center for a C12-AHL spherical aggregate with 20 AHLs. The distribution was computed using the last 5 ns of the equilibration trajectory. The dashed red line indicates the aggregate radius, defined using this plot, that was compared to experimental TEM measurements.

The diameters of the spherical aggregates were estimated from the last 5 ns of the equilibration run. The diameter was defined using the distribution of head group lactone ring oxygen atom as function of the radial distance from the aggregate COM (Figure S8B). The diameter was defined as twice the radial distance for which (*i*) the radial distance was greater than the distance corresponding to the peak of the distribution and (*ii*) the value of the distribution fell below 0.003. Distributions of oxygen atoms were calculated in a similar way to distributions of AHL center of masses discussed in section S6.

Table S1. Spherical aggregate sizes estimated from simulations.

	Diameter of spherical aggregate (nm)		
AHL	20 molecules	50 molecules	100 molecules
C8-AHL	*4.1*	*4.8*	*6.0*
C10-AHL	*4.1*	*4.9*	*6.1*
C12-AHL	*4.2*	*5.1*	*6.2*
C14-AHL	*4.2*	*5.1*	*6.2*
C16-AHL	*4.3*	*5.2*	*6.3*
3-oxo-C10-AHL	*4.5*	*5.3*	*6.9*
3-oxo-C12-AHL	*4.0*	*4.5*	*5.9*
3-oxo-C14-AHL	*4.5*	*5.5*	*6.6*
3-oxo-C16-AHL	*4.6*	*6.0*	*6.5*

Section S8. Determination of free energy change for aggregation from alchemical free energy calculations

The values of $\Delta\mu_{aggr}$ from the alchemical free energy calculations plotted in Figure 6 of the main text are listed in Table S2. The errors in the free energies are the standard deviation as estimated by the alchemical free energy calculation tool.[9] Table S2 also lists $\Delta\mu_{aggr}$ computed from alchemical free energy calculations for spherical and bilayer aggregates of the zwitterionic lipid POPC. POPC is included as a control it prefers a bilayer structure and thus the bilayer should have a lower value of $\Delta\mu_{aggr}$ than spherical aggregates. Because of the larger system size required for the POPC systems (due to the molecular size of the lipids), simulations of cylindrical aggregates were not performed.

Table S2. $\Delta\mu_{aggr}$ calculated for each AHL for spherical aggregates with 20, 50 and 100 AHLs, cylinders, and bilayers. All values are reported in kJ/mol. ** indicates that the simulation was not performed because the system was unable to maintain the indicated structure during equilibration (or due to computational expense in the case of the POPC cylinder).

AHL	$\Delta\mu_{aggr}$ (kJ/mol)				
	Sphere (20 molecules)	***Sphere (50 molecules)***	***Sphere (100 molecules)***	***Cylinder***	***Bilayer***
POPC	*-60.9 ± 0.8*	*-72.3 ± 1.1*	**	**	*-88.3 ± 1.5*
C8-AHL	*-20.5 ± 0.3*	*-21.0 ± 0.2*	*-27.5 ± 0.3*	*-29.9 ± 0.3*	**
C10-AHL	*-25.8 ± 0.3*	*-32.9 ± 0.3*	*-28.3 ± 0.4*	*-31.7 ± 0.3*	*-34.4 ± 0.4*
C12-AHL	*-30.6 ± 0.4*	*-35.2 ± 0.4*	*-39.0 ± 0.3*	*-31.1 ± 0.3*	*-34.4 ± 0.5*
C14-AHL	*-34.5 ± 0.3*	*-43.3 ± 0.3*	*-37.3 ± 0.3*	*-46.3 ± 0.4*	*-51.1 ± 0.7*
C16-AHL	*-42.2 ± 0.4*	*-43.4 ± 0.3*	*-49.2 ± 0.4*	*-55.8 ± 0.5*	*-74.2 ± 0.3*
3-oxo-C10-AHL	*-16.9 ± 0.5*	*-20.5 ± 0.3*	*-25.9 ± 0.1*	*-21.3 ± 0.3*	**
3-oxo-C12-AHL	*-23.1 ± 0.4*	*-29.4 ± 0.5*	*-30.6 ± 0.2*	*-31.2 ± 0.5*	*-25.8 ± 0.4*
3-oxo-C14-AHL	*-27.0 ± 0.3*	*-30.4 ± 0.3*	*-29.6 ± 0.5*	*-39.2 ± 0.4*	*-40.6 ± 0.5*
3-oxo-C16-AHL	*-34.0 ± 0.4*	*-38.5 ± 0.4*	*-41.9 ± 0.5*	*-44.4 ± 0.4*	*-77.1 ± 0.3*

Section S9. Analysis of aggregate sizes from TEM images

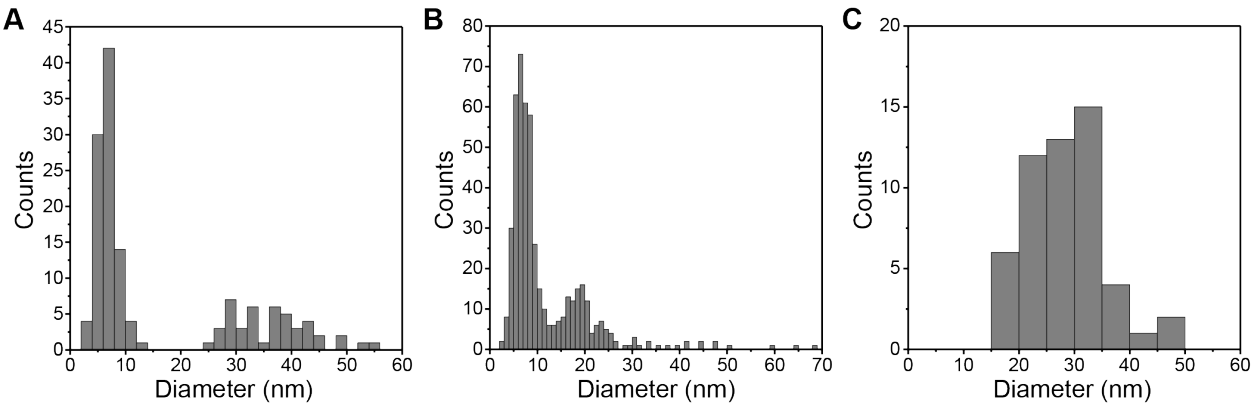

Figure S9. Histograms showing the distribution of diameters measured for aggregates observed in TEM images of samples prepared from solutions of AHLs. (A) Aggregates observed in 100 μM solutions of 3-oxo-C12-AHL (140 aggregates measured from the images shown in Figures 8A and 8B, and 3 additional images). (B) Aggregates observed in 6.25 μM and 12.5 μM solutions of C12-AHL (490 aggregates measured from the images shown in Figures 8C, 8D, and S12D; small and large aggregates were observed in solutions at both concentrations). (C) Aggregates observed in 1 μM solutions of C12-AHL (53 aggregates measured from the image displayed in Figure 8E).

The diameters of the aggregates imaged by TEM were measured using NIH ImageJ and reported in the histograms in Figure S9. The scale of the image was set by measuring the width of the scale bar generated by the TEM software in pixels and converting that to the appropriate physical length. The diameters of the aggregates imaged were then measured by drawing a straight line across the equator of the aggregates and measuring the length of that line. For particles that were oblong, the long axis of the particles was measured, which could lead to an overestimate in particle size. To determine the sizes of "small" and "large" aggregates found in solutions of 3-oxo-C12-AHL and C12-AHL (see main text), particles smaller than 13 nm and 12 nm respectively were considered "small" aggregates and aggregates larger than those values were designated as "large" aggregates. These values were chosen because they represent natural break points between the two modes of the distributions observed in the histogram.

Section S10. Characterization of aggregate sizes in solution of AHLs using DLS

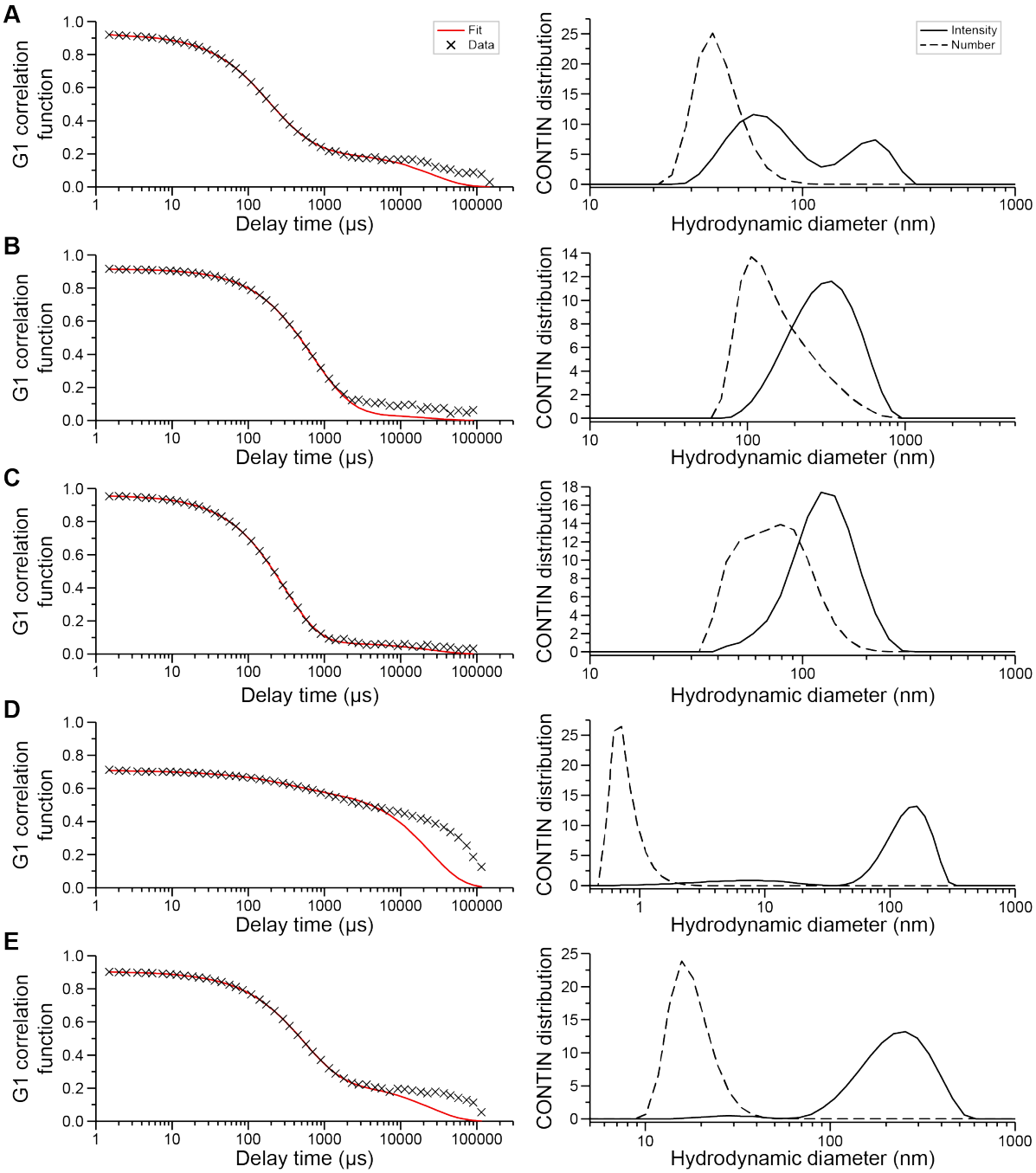

Figure S10. Results of DLS analyses of aggregates present in solutions of AHLs. (Left) Autocorrelation functions (ACFs) and corresponding CONTIN fits to the ACFs and (Right) Corresponding intensity and number averages size distributions for aggregated structures found in: (A) 3000 µM 3-oxo-C8-AHL, (B) 10 µM C12-AHL, (C) 5 µM C16-AHL and (D and E) 125 µM 3-oxo-C12-AHL. As also stated in the main text, and observed in this figure, CONTIN analysis poorly fits the raw autocorrelation function for 3-oxo-C12-AHL. While the CONTIN intensity and number average distributions for this molecule are displayed in the figure, they are only included to show the bimodal nature of the data, not for the determination of an aggregate size.

Section S11. Additional TEM images

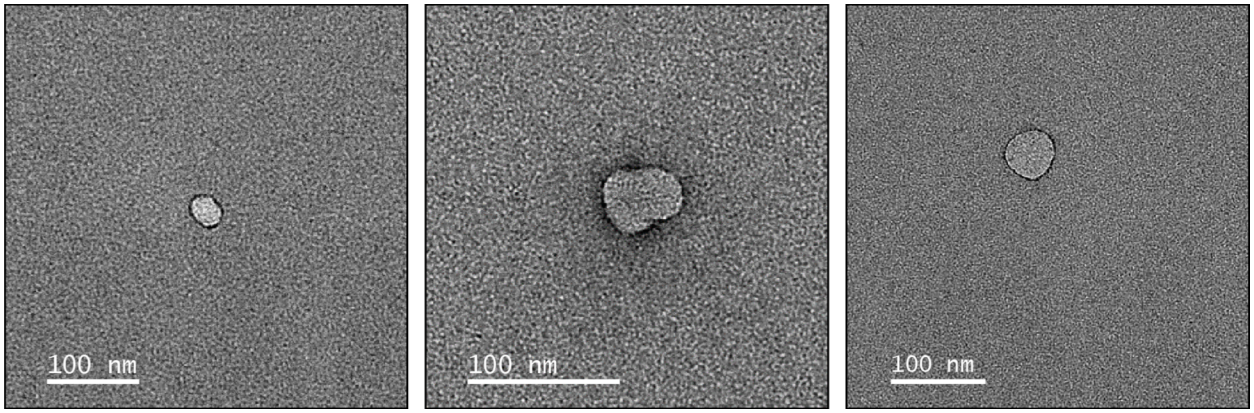

Figure S11. TEM images showing representative aggregates found in 3000 μM solutions of 3-oxo-C8-AHL.

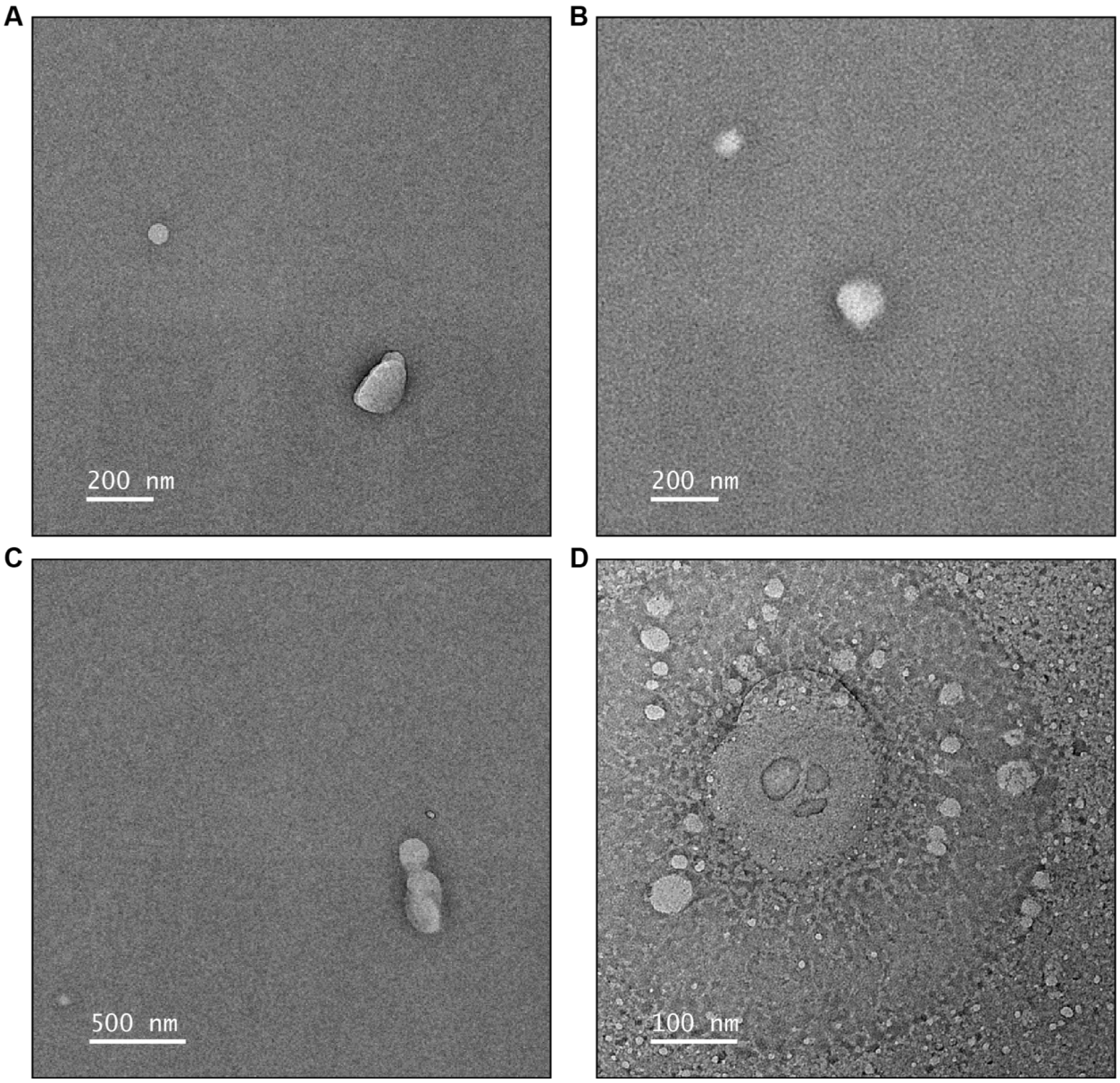

Figure S12. TEM images showing representative views of the largest aggregates found in (A-C) 50 μM C12-AHL solutions and (D) 6.25 μM C12-AHL solution. The aggregates shown in (A-C) roughly correspond to the sizes of aggregates observed by DLS in solutions of C12-AHL.

References

1. Lin, S. Y.; Lin, Y. Y.; Chen, E. M.; Hsu, C. T.; Kwan, C. C., A Study of the Equilibrium Surface Tension and the Critical Micelle Concentration of Mixed Surfactant Solutions. *Langmuir* **1999,** *15* (13), 4370-4376.
2. Chen, L. J.; Lin, S. Y.; Huang, C. C.; Chen, E. M., Temperature Dependence of Critical Micelle Concentration of Polyoxyethylenated Non-Ionic Surfactants. *Colloids Surf., A* **1998,** *135* (1-3), 175-181.
3. Patist, A.; Bhagwat, S. S.; Penfield, K. W.; Aikens, P.; Shah, D. O., On the Measurement of Critical Micelle Concentrations of Pure and Technical-Grade Nonionic Surfactants. *J. Surfactants Deterg.* **2000,** *3* (1), 53-58.
4. Martinez, L.; Andrade, R.; Birgin, E. G.; Martinez, J. M., Packmol: A Package for Building Initial Configurations for Molecular Dynamics Simulations. *J. Comput. Chem.* **2009,** *30* (13), 2157-64.
5. Haverkort, F.; Stradomska, A.; de Vries, A. H.; Knoester, J., Investigating the Structure of Aggregates of an Amphiphilic Cyanine Dye with Molecular Dynamics Simulations. *J. Phys. Chem. B* **2013,** *117* (19), 5857-5867.
6. Israelachvili, J. N., *Intermolecular and Surface Forces*. 3rd ed.; Academic Press: 2011.
7. Jakobtorweihen, S.; Yordanova, D.; Smirnova, I., Predicting Critical Micelle Concentrations with Molecular Dynamics Simulations and Cosmomic. *Chem. Ing. Tech.* **2017,** *89* (10), 1288-1296.
8. Shirts, M. R.; Chodera, J. D., Statistically Optimal Analysis of Samples from Multiple Equilibrium States. *J. Chem. Phys.* **2008,** *129* (12).
9. Klimovich, P. V.; Shirts, M. R.; Mobley, D. L., Guidelines for the Analysis of Free Energy Calculations. *J. Comput.-Aided Mol. Des.* **2015,** *29* (5), 397-411.
10. Wijmans, C. M.; Eiser, E.; Frenkel, D., Simulation Study of Intra- and Intermicellar Ordering in Triblock-Copolymer Systems. *J. Chem. Phys.* **2004,** *120* (12), 5839-5848.